Journal of Materials Chemistry A

ROYAL SOCIETY OF CHEMISTRY

PAPER

View Article Online
View Journal | View Issue

Cite this: J. Mater. Chem. A, 2025, 13, 26337

Engineering redox-active benzo[1,2-*b*:4,5-*b*′] dithiophene-based conjugated polymers: tuning porosity and linker architecture for high-performance supercapacitors†

Yousra M. Nabil,[ab] Shimaa Abdelnaser,[ab] Ahmed A. K. Mohammed,[b] Shiao-Wei Kuo [a] and Ahmed F. M. EL-Mahdy *[ab]

Conjugated polymers have emerged as promising candidates for next-generation supercapacitor electrodes due to their high conductivity, redox activity, and π-conjugated frameworks. In this work, we conduct a comprehensive investigation into how porosity and linker architecture affect the electrochemical properties of four conjugated polymers that incorporate the redox-active benzo[1,2-b:4,5-b′]dithiophene-4,8-dione (DTDO) units. Specifically, two types of porous polymers (Ph-DTDO porous and TEPh-DTDO porous) and two types of linear polymers (Ph-DTDO linear and DEPh-DTDO linear) are synthesized using Suzuki and Sonogashira coupling reactions, employing structurally tailored phenyl-based linkers. Among them, the Ph-DTDO porous conjugated polymer demonstrates superior performance, delivering a high specific capacitance of 842.4 F g^{-1} at 0.5 A g^{-1} and excellent stability with 98.78% retention after 6000 cycles in a three-electrode system. Furthermore, the symmetric supercapacitor device assembled with the Ph-DTDO porous polymer exhibits an energy density of 59.4 W h kg^{-1} and a specific capacitance of 428.21 F g^{-1}. Comparative analysis reveals that the porous architecture and phenyl-bridged linker facilitate enhanced ion diffusion, higher capacitive contribution, lower charge transfer resistance, and improved π–π stacking interactions, thus significantly boosting the energy storage capabilities. This work underscores the crucial role of structural engineering in conjugated polymers and offers valuable design insights for high-performance energy storage materials.

Received 15th May 2025
Accepted 1st July 2025

DOI: 10.1039/d5ta03907j

rsc.li/materials-a

1. Introduction

The interruption of renewable energy sources such as solar and wind power has created a demand for effective, readily available, and safe energy storage systems.[1] Recently, there has been an imperative need for energy storage systems, including batteries and supercapacitors (SCs) that exhibit enhanced mechanical and electrochemical stability, as well as improved flexibility.[2] Despite the remarkable power density of supercapacitors compared with batteries, researchers are still using advanced electrode materials containing carbon doped with S, O, B, P, N, –NH, –OH, *etc.* to improve capacitor efficiency.[3–5] Supercapacitors are categorized into three main types based on different materials and mechanisms:[6] Electrochemical double-layer capacitors (EDLCs), pseudocapacitors, and hybrid capacitors. EDLC arises from the adsorbed and desorbed electrolyte ions on the electrode surface. Carbon-based materials such as carbon nanotubes (CNTs), graphene, and activated carbon are widely used in electric double-layer capacitors (EDLCs) due to their outstanding electrical conductivity, excellent cycling stability, large specific surface area, and cost-effectiveness.[7] However, despite their high power density and exceptional rate capability, carbon-based supercapacitors suffer from low energy density and limited specific capacitance, primarily due to the lack of intrinsic redox-active sites.[8,9] In contrast, pseudocapacitance involves ions occupying tunnels or empty positions within the bulk material.[10] Metal oxides and conductive polymers are pseudocapacitive materials that utilize faradaic redox processes to store energy.[8,11] However, the rapid redox reactions in many pseudocapacitive materials often lead to volumetric expansion and contraction of the electrodes, compromising their mechanical integrity and limiting access to active sites.[12] Moreover, their inherently low rate capability, poor electrical conductivity, and limited cycling stability hinder their practical application.[13] To address these challenges, integrating transition-metal oxides and conductive polymers into hybrid and heterostructured systems has shown significant promise in enhancing ion/electron transport, electrochemical stability, and

[a]*Department of Materials and Optoelectronic Science, National Sun Yat-Sen University, Kaohsiung 80424, Taiwan. E-mail: ahmedelmahdy@mail.nsysu.edu.tw*

[b]*Chemistry Department, Faculty of Science, Assiut University, Assiut 71516, Egypt*

† Electronic supplementary information (ESI) available. See DOI: https://doi.org/10.1039/d5ta03907j

overall performance.[14] Hybrid capacitors merge both EDLC and pseudocapacitance to attain much improved energy density and broader operational potential windows.[7,10,15,16] Enhancing the capacitance performance of SCs relies on various factors, including improvements to the electrolytes, current collectors, and electrode specific surface area.[17,18] Therefore, addressing these limitations requires the development of next-generation electrode materials that possess intrinsic electrical conductivity, precisely tunable porosity, robust structural stability, and strategically integrated redox-active moieties to enable enhanced supercapacitor performance. Moreover, a comprehensive understanding of the structure–performance relationship of electrode materials is essential for the rational design and development of high-performance supercapacitor electrodes.

Conjugated polymers are a highly adaptable class of organic materials that have garnered increasing attention for energy storage applications, mainly due to their intrinsic electrical conductivity, redox activity, and flexible molecular design.[19–21] These materials have been extensively explored in various other fields, including gas storage and separation,[22–24] heterogeneous catalysis,[22,25] solar energy conversion,[26] optoelectronic sensing,[27,28] photocatalysis for environmental remediation,[29–31] and electrochemical energy storage devices such as supercapacitors.[19,32] Conjugated polymers can be broadly categorized into porous and linear systems, each offering distinct yet complementary structural features that contribute to their effectiveness as supercapacitor electrode materials.[33] (1) Porous conjugated polymers, such as conjugated microporous polymers (CMPs), consist of rigid, cross-linked networks that incorporate extended π-conjugated backbones and permanent microporosity.[34,35] This structural configuration facilitates rapid ion diffusion, high surface accessibility, and effective charge transport—attributes that are critical for enhancing specific capacitance and rate performance.[36] For example, a carbazole-based CMP synthesized *via* Suzuki coupling was reported to deliver a specific capacitance exceeding 271 F g^{-1}, owing to its high surface area and well-distributed redox-active sites.[37] In contrast, (2) linear conjugated polymers are composed of well-defined, non-crosslinked chains that exhibit superior charge carrier mobility due to uninterrupted π-conjugation along the backbone.[27] Their inherent redox reversibility, ease of film formation, and compatibility with flexible substrates make them excellent candidates for pseudocapacitive energy storage. An illustrative example is poly(3,4-ethylenedioxythiophene) (PEDOT), a widely studied linear conjugated polymer, which demonstrates high electrical conductivity and a specific capacitance of over 171 F g^{-1} under optimized conditions.[38] Both porous and linear conjugated polymers can be synthesized using various coupling strategies, including Suzuki, Sonogashira, and Buchwald–Hartwig reactions, enabling precise control over their molecular architecture and functional properties.[35,39–41] Therefore, a comprehensive understanding of the structure–property relationships in these materials is crucial for guiding the rational design of next-generation supercapacitor electrodes that combine high energy and power densities with excellent operational efficiency and stability.

In this study, we systematically investigate the influence of porosity and linker architecture on the supercapacitor performance of conjugated polymer-based electrode materials. To this end, four conjugated polymers were rationally designed and synthesized, incorporating the redox-active benzo[1,2-*b*:4,5-*b*′] dithiophene-4,8-dione (DTDO) unit as the electron-deficient core.[42] The polymer series includes two porous frameworks—Ph-DTDO porous and TEPh-DTDO porous—and two linear analogues—Ph-DTDO linear and DEPh-DTDO linear. Structural diversity was achieved by employing distinct linker motifs: benzene and ethynylbenzene, allowing for a comparative analysis of how molecular architecture (porous *vs.* linear) and linker type (benzene and ethynylbenzene) influence the electrochemical behavior and capacitive performance. Ph-DTDO porous and TEPh-DTDO porous polymers were synthesized *via* Suzuki and Sonogashira coupling reactions, respectively, using 2,6-dibromobenzo[1,2-*b*:4,5-*b*′]dithiophene-4,8-dione (DTDO-2Br) with benzene-1,3,5-triyltriboronic acid [Ph-3B$(OH)_2$] and 1,3,5-triethynylbenzene (TEPh-3C≡C). In contrast, the linear analogues—Ph-DTDO linear and DEPh-DTDO linear—were prepared by coupling DTDO-2Br with 1,4-phenylenediboronic acid [Ph-2B$(OH)_2$] and 1,4-diethynylbenzene (DEPh-2C≡C),

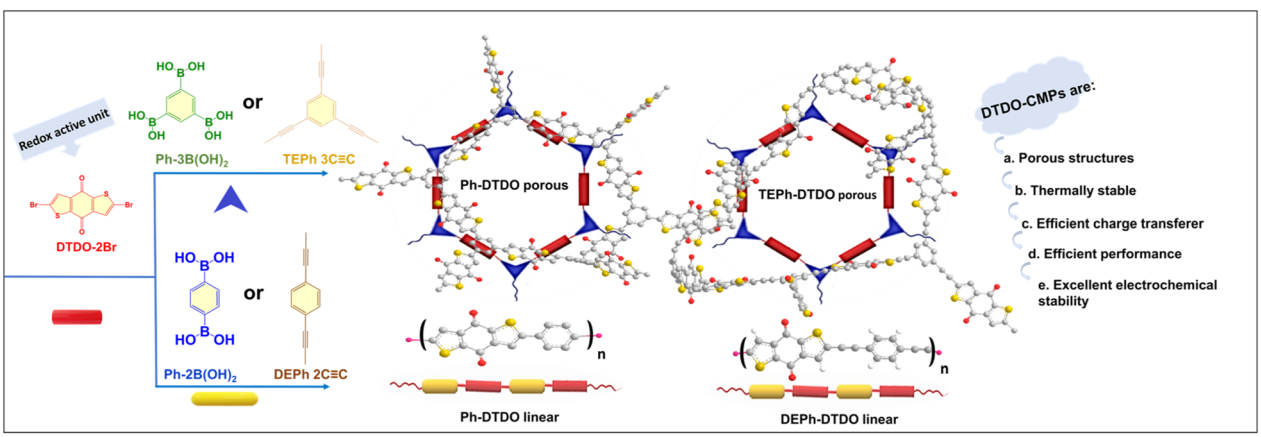

Fig. 1 Synthetic routes and molecular structures of DTDO-based conjugated polymers.

respectively, as illustrated in Fig. 1. Among them, the Ph-DTDO porous polymer exhibited excellent electrochemical performance, delivering a high specific capacitance of 842.4 F g^{-1} and outstanding cycling stability (98.78% retention after 6000 cycles) in a three-electrode system. In a symmetric device, it achieved 428.21 F g^{-1} and 59.4 W h kg^{-1} energy density, maintaining 88.51% capacitance after 4000 cycles. The superior electrochemical performance of the Ph-DTDO porous polymer is primarily attributed to its high surface area and intrinsic porosity, which facilitate efficient ion diffusion and rapid charge transport. Moreover, the incorporation of a benzene-based linker promotes a fully aromatic framework, enhancing π–π stacking interactions between polymer layers. This structural arrangement significantly improves charge carrier mobility, resulting in an elevated electrical conductivity of up to 5.88 S cm^{-1}. These findings underscore the pivotal role of porous architecture, enhanced π–π stacking interactions, and efficient charge-transfer pathways enabled by the molecular linkers in governing the electrochemical performance of the materials.

2. Results and discussion

2.1. Synthesis and characteristics of materials

The synthetic strategy and structural diversity of the DTDO-based conjugated polymers are illustrated in Fig. 1. The redox-active core, 2,6-dibromobenzo[1,2-b:4,5-b′]dithiophene-4,8-dione (DTDO-2Br, Scheme S1 and Fig. S1–S3†), was employed as the electron-deficient building unit in all polymer frameworks. To construct porous and linear architectures, DTDO-2Br was polymerized with different linker motifs *via* Suzuki and Sonogashira–Hagihara coupling reactions. Specifically, Ph-3B$(OH)_2$ and TEPh-3C≡C were used to generate Ph-DTDO porous and TEPh-DTDO porous conjugated polymers, while Ph-2B$(OH)_2$ and DEPh-2C≡C were used to form the linear analogues, Ph-DTDO linear and DEPh-DTDO linear conjugated polymers (Fig. 1 and Schemes S2–S5†). The porous polymers exhibited cross-linked frameworks with intrinsic microporosity, whereas the linear polymers adopted well-defined, one-dimensional π-conjugated backbones. The synthesized DTDO-conjugated polymers, whether crosslinked or linear, were insoluble in typical organic solvents such as THF, acetone, and DMF. Rather than dissolving, these polymers form stable suspensions upon dispersion, as illustrated in Fig. S4.†

Various techniques were employed to assess the chemical composition of the synthesized DTDO-conjugated polymers such as FTIR, solid-state ^{13}C cross polarization (CP)/magic angle spinning (MAS) NMR, and X-ray photoelectron spectroscopy (XPS). The FTIR spectra of the Ph-DTDO porous, Ph-DTDO linear, TEPh-DTDO porous, and DEPh-DTDO linear polymers confirmed the successful formation of the desired polymers. Specifically, the absence of the characteristic C–Br stretching vibration at 580 cm^{-1}, originally present in the DTDO-2Br monomer, indicated the complete consumption of the brominated precursor in all synthesized polymers (Fig. S5–S8†). Additionally, the disappearance of the B–O stretching vibration at 1333 cm^{-1} in both Ph-DTDO porous and Ph-DTDO linear polymers supported the full progress of the Suzuki polymerization reaction (Fig. S5 and S6†). In contrast, the FTIR spectra of the TEPh-DTDO porous and DEPh-DTDO linear polymers showed the disappearance of the terminal alkyne (C≡C–H) stretching vibrations at 3264–3281 cm^{-1}, which are characteristic of the monomers DEPh–2C≡C and TEPh–3C≡C. Meanwhile, the retention of the internal C≡C stretching band confirmed the successful formation of the conjugated polymer backbone through Sonogashira–Hagihara coupling (Fig. S7 and S8†). Furthermore, all DTDO-based conjugated polymers exhibited characteristic C=O carbonyl stretching bands between 1645 and 1660 cm^{-1}, while the aromatic C–H and C=C vibrations were observed in the regions of 3044–3131 cm^{-1} and 1406–1535 cm^{-1}, respectively. For the TEPh-DTDO porous and DEPh-DTDO linear polymers, the internal C≡C stretching band appeared at 2192 and 2188 cm^{-1}, respectively (Fig. S7 and S8†). The solid-state ^{13}C NMR spectra of the DTDO-based conjugated polymers (Fig. 2a) revealed three distinct resonance regions located at 175.8–175.09, 153.98–137.65, and 133.84–118.24 ppm, which were attributed to carbonyl (C=O), aromatic C–X (X = C or S), and aromatic C–H carbon atoms, respectively.

To confirm the elemental composition of the DTDO-based conjugated polymers, XPS analysis was performed. As shown in Fig. S9,† no extraneous elements were detected, indicating the absence of detectable impurities in the conjugated polymers during synthesis. The spectra further revealed the presence of four distinct peaks corresponding to S 2p, S 2s, C 1s, and O 1s orbitals. For the Ph-DTDO porous polymer, these peaks appeared at binding energies of 160.85, 227.84, 283.88, and 531.28 eV, respectively. In contrast, the Ph-DTDO linear polymer exhibited the respective peaks at 163.55, 227.45, 284.04, and 530.46 eV. Furthermore, the XPS spectrum of the TEPh-DTDO porous polymer revealed elemental peaks at 164.15, 227.64, 284.04, and 531.28 eV, corresponding to the S 2p, S 2s, C 1s, and O 1s orbitals, respectively. Similarly, for the DEPh-DTDO linear polymer, the respective peaks were detected at 163.95, 227.54, 283.96, and 530.87 eV, respectively (Fig. S9†). To gain a clear insight into the types of element species present in the conjugated polymers, we fitted the XPS patterns for the C 1s orbitals (Fig. 2b–e, Tables S1 and S2†). The C 1s spectrum for the Ph-DTDO porous polymer was deconvoluted into four distinct peaks at 283.79 eV for C=C, 284.05 eV for C–S, 284.62 eV for C–C, and 286.56 eV for C=O (Fig. 2b and Tables S1, S2†). Furthermore, C 1s for Ph-DTDO linear was modeled with four peaks at 283.49, 284.02, 284.50, and 286.50 for C=C, C–S, C–C, and C=O chemical bonds respectively (Fig. 2c, Tables S1 and S2†). Additionally, the C 1s spectrum of the TEPh-DTDO porous polymer exhibited five peaks at 283.74, 284.04, 284.05, 284.98, and 286.66 eV, corresponding to C=C, C–S, C–C, C≡C, and C=O bonds (Fig. 2d, Tables S1 and S2†). Similarly, the DEPh-DTDO linear polymer showed peaks at 283.63, 284.10, 284.43, 284.47, and 286.54 eV, assigned to the same bonding environments (Fig. 2e, Tables S1 and S2†). The S 2p spectra exhibited two characteristic peaks corresponding to the S $2p_{3/2}$ and S $2p_{1/2}$ spin–orbit components in a 2 : 1 intensity ratio. These peaks were observed at 163.58 and 164.77 eV for the Ph-DTDO porous polymer, 163.29 and 164.49 eV for the Ph-DTDO linear polymer,

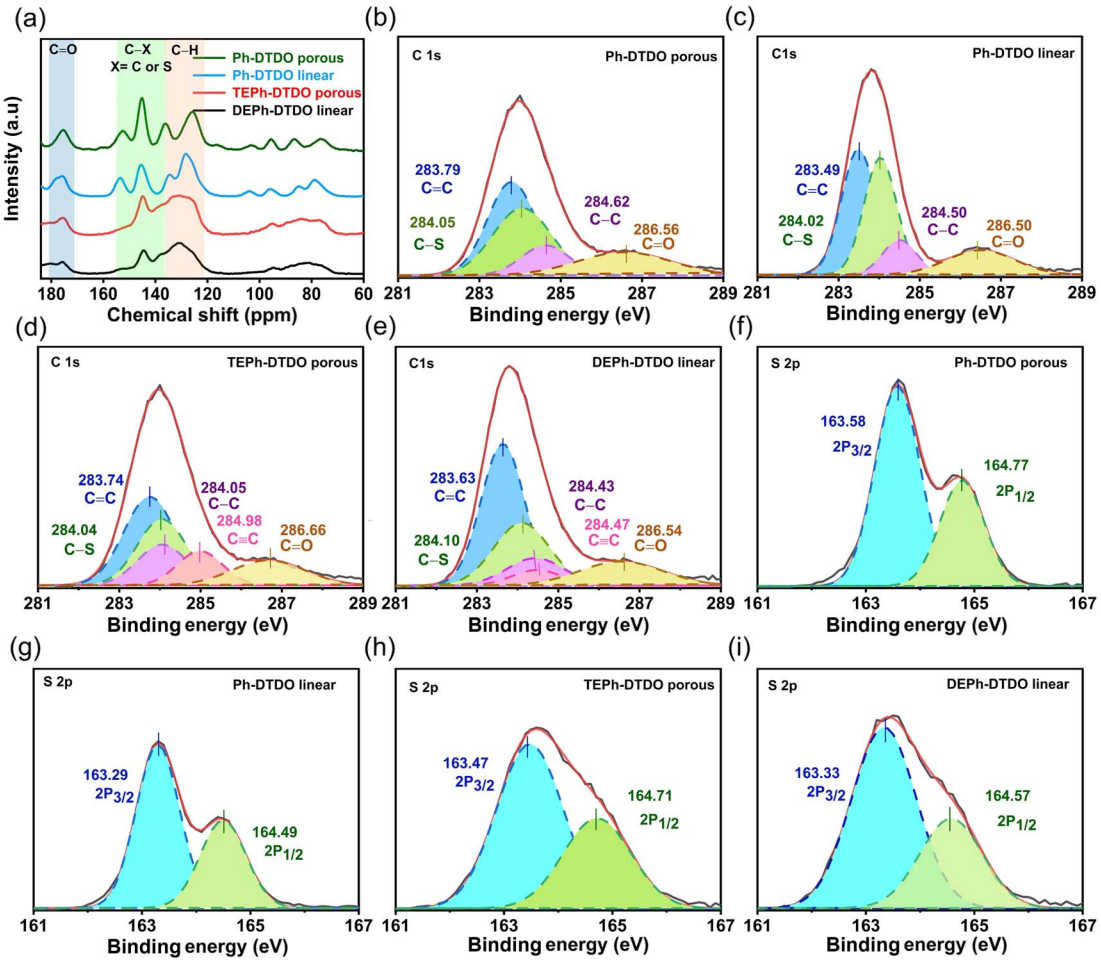

Fig. 2 (a) ^{13}C CP-MAS NMR spectra of the Ph-DTDO porous, Ph-DTDO linear, TEPh-DTDO porous, and DEPh-DTDO linear conjugated polymers. (b–i) High resolution XPS (b–e) C 1s spectra and (f–i) S 2p spectra of the Ph-DTDO porous, Ph-DTDO linear, TEPh-DTDO porous, and DEPh-DTDO linear conjugated polymers.

163.47 and 164.71 eV for the TEPh-DTDO porous polymer, and 163.33 and 164.57 eV for the DEPh-DTDO linear polymer (Fig. 2f–i, Tables S1 and S2†). As displayed in Table S2† the XPS percentages of C–S in the Ph-DTDO porous and Ph-DTDO linear polymers are 32.62% and 34.86% respectively, higher than those of the other TEPh-DTDO porous and DEPh-DTDO linear polymers at 24.69% and 24.93%, suggesting the enhanced capacitance characteristics of the Ph-DTDO porous and Ph-DTDO linear polymers.[43]

A range of characterization techniques, including nitrogen adsorption–desorption isotherms, thermogravimetric analysis (TGA), and X-ray diffraction (XRD), were employed to evaluate the porosity, thermal stability, and crystallinity of the synthesized DTDO-based conjugated polymers. The standard procedure for assessing the porosity of the Ph-DTDO porous and TEPh-DTDO porous conjugated polymers is through nitrogen gas adsorption and desorption analysis (Fig. 3a). The data gathered from these measurements were subsequently examined utilizing Brunauer–Emmett–Teller (BET) theory as evident in Fig. 3a and Table S3.† The nitrogen adsorption–desorption isotherms of the Ph-DTDO porous and TEPh-DTDO porous conjugated polymers correspond to type II behavior, characterized by pronounced nitrogen uptake at low relative pressures ($P/P_0 < 0.1$) and again at high pressures ($P/P_0 > 0.89$), indicative of the coexistence of micro- and mesoporous structures. As illustrated in Fig. 3a and summarized in Table S3,† the pore size distribution for the Ph-DTDO porous polymer showed a broad peak spanning 1.65–3.41 nm, while the TEPh-DTDO porous polymer displayed a distribution from 1.58–3.77 nm. In terms of surface textural properties, the Ph-DTDO porous polymer exhibited a BET surface area of 62.7 $m^2\ g^{-1}$ and a pore volume of 0.36 $cm^3\ g^{-1}$, whereas the TEPh-DTDO porous polymer achieved a higher surface area of 92.3 $m^2\ g^{-1}$ and a pore volume of 0.43 $cm^3\ g^{-1}$. Therefore, it can be inferred that the DTDO-porous conjugated polymers have considerable surface area, indicating enhanced porosity with surface reactivity capability. Additionally, we performed TGA to investigate the thermal stability of these fabricated polymers, by exposing the polymer samples to temperatures ranging from 40 to 800 °C in a N_2 atmosphere. Fig. 3b and Table S4† verified their remarkable thermal stability as the decomposition temperatures at 5% wt of the Ph-DTDO porous, Ph-DTDO linear, TEPh-DTDO porous, and DEPh-DTDO linear conjugated polymers were 425.50, 536.64, 359.64, and 310.20 °C, respectively, even though

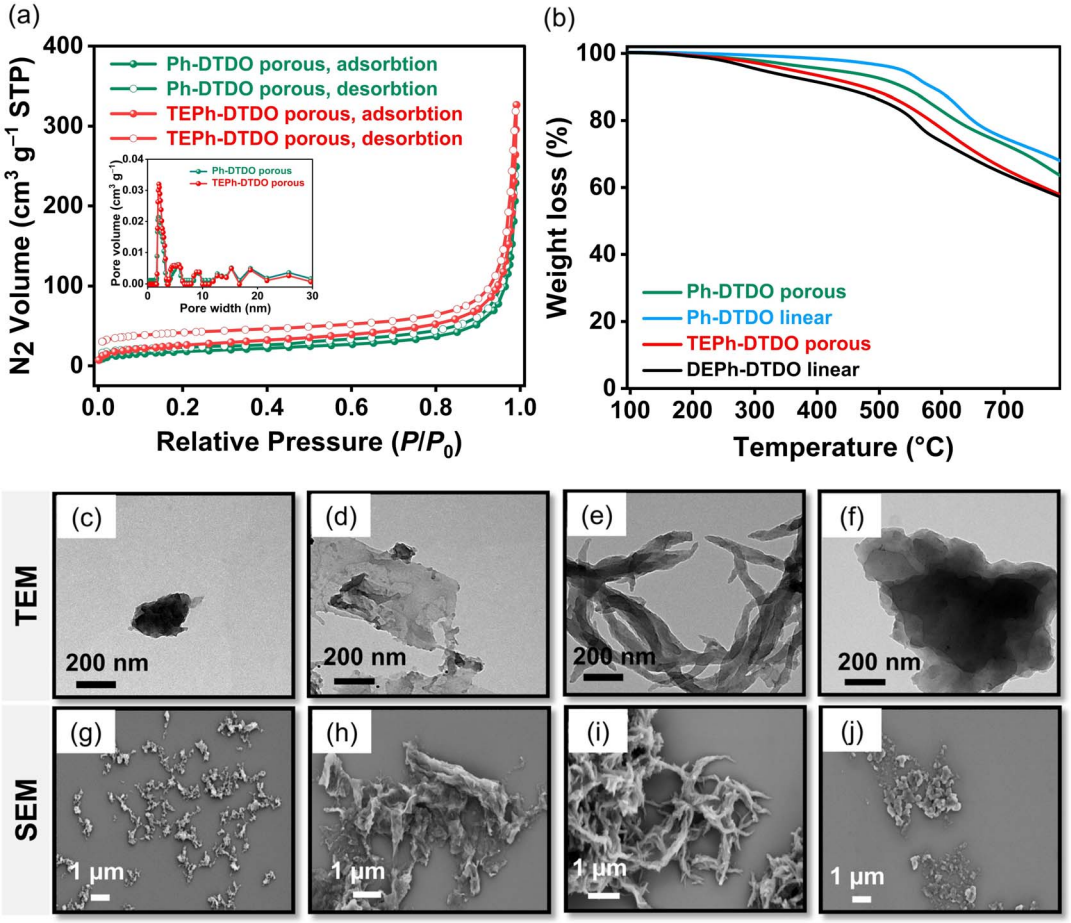

Fig. 3 (a) N_2 adsorption/desorption isotherms and pore size distribution curves for the Ph-DTDO porous and TEPh-DTDO porous polymers. (b) TGA spectra, (c–f) TEM images, and (g–j) SEM images for the Ph-DTDO porous, Ph-DTDO linear, TEPh-DTDO porous, and DEPh-DTDO linear polymers.

their decomposition temperatures at 10% wt were 537.94, 583.71, 474.66, and 434.57 °C, respectively. Remarkably, upon heating to 800 °C, the residual masses are recorded as 63.50, 67.93 and 57.76, and 57.14% for the Ph-DTDO porous, Ph-DTDO linear, TEPh-DTDO porous, and DEPh-DTDO linear conjugated polymers, respectively. In contrast to the TEPh-DTDO porous and DEPh-DTDO linear polymers, the Ph-DTDO porous and Ph-DTDO linear conjugated polymers demonstrated greater improved thermal stability due to the inclusion of a phenyl bridge in their framework, which contributes to their thermal stability enhancement.[44] Furthermore, the powder XRD patterns of the synthesized DTDO-based conjugated polymers were analyzed. Fig. S10a† shows broad signals, suggesting that they are amorphous and do not possess long-range structural features, as previously mentioned.[22,45,46] From the XRD spectrum we determined the interlayer distance (π–π stacking) using Bragg's Law (eqn (1)).

$$n\lambda = 2d\sin(\theta) \quad (1)$$

Notably, π–π stacking interactions are often evidenced by a broad diffraction peak observed in the 2θ range of 20° to 25°, which corresponds to an interlayer distance of approximately 3.5–4.5 Å. This characteristic feature has been reported in numerous studies and can be detected in both crystalline and amorphous organic materials, as it arises from the regular arrangement or close packing of conjugated aromatic units, regardless of long-range structural order. Such broad peaks are commonly used as indicators of short-range π–π stacking in polymeric and molecular systems.[47–50] The calculated interlayer π–π stacking distances for Ph-DTDO porous, Ph-DTDO linear, TEPh-DTDO porous, and DEPh-DTDO linear polymers were 0.38, 0.33, 0.39, and 0.37 Å, respectively (Fig. S10b–e†). Notably, the Ph-DTDO porous polymer exhibits a shorter π–π stacking distance than TEPh-DTDO porous, and similarly, Ph-DTDO linear shows a smaller stacking distance compared to DEPh-DTDO linear. These observations suggest that the benzene linker in Ph-DTDO-based polymers facilitates stronger π–π interactions than the ethynylbenzene linker.

2.2. Morphology studies

The morphological and elemental analysis of the four DTDO-based polymers—Ph-DTDO porous, Ph-DTDO linear, TEPh-DTDO porous, and DEPh-DTDO linear—were carried out

using transmission electron microscopy (TEM), scanning electron microscopy (SEM), and energy-dispersive X-ray spectroscopy (EDS) mapping (Fig. 3c–j, S11 and S12†). TEM imaging shows that each of the Ph-DTDO porous, Ph-DTDO linear, and DEPh-DTDO linear conjugated polymers displays sheet-like structures or flake morphologies with rough and irregular textures. Conversely, the TEPh-DTDO porous polymer adopts a rod-like structure. SEM images further support these observations (Fig. 3c–j and S11†). The corresponding EDS elemental mapping confirms the homogeneous distribution of carbon (C), oxygen (O), and sulfur (S) elements in all four polymers, verifying the successful incorporation of the designed molecular components (Fig. S12†). Notably, the TEPh-DTDO porous sample displays a well-defined nanosheet morphology, which can be attributed to the specific reaction conditions employed, particularly the use of a DMF/TEA solvent mixture. Additionally, the Sonogashira coupling between aryl halides and terminal alkynes further contributes to the formation of this distinctive structure.[51]

2.3. Electrochemical properties

The electrochemical performance of the DTDO-based conjugated polymers was systematically evaluated using cyclic voltammetry (CV) and galvanostatic charge–discharge (GCD) measurements in a three-electrode setup (Fig. 4). These measurements were conducted in 3 M KOH aqueous electrolyte, where a glassy carbon electrode served as the working electrode, platinum wire as the counter electrode, and a Hg/HgO electrode as the reference. CV curves were recorded over a range of scan rates from 5 to 200 mV s^{-1} to investigate the redox behavior of the materials. The quasi-rectangular CV profiles with distinct redox peaks indicate pronounced pseudocapacitive behavior arising from Faradaic charge-transfer processes in all synthesized conjugated polymers (Fig. 4a–d). At a scan rate of 5 mV s^{-1}, the Ph-DTDO porous polymer exhibited oxidation and reduction peak potentials at approximately −0.31 V and −0.40 V, respectively. For the Ph-DTDO linear polymer, these peaks were observed at −0.48 V and −0.51 V. The TEPh-DTDO porous polymer displayed corresponding redox peaks at −0.31 V and −0.34 V, while the DEPh-DTDO linear polymer showed peaks at −0.29 V and −0.38 V, respectively (Fig. 4a–d). The CV curves of the synthesized conjugated polymers maintained their characteristic shape across a range of scan rates, indicating excellent capacitive behavior and fast charge–discharge kinetics.[52] The distinct redox peak profiles observed in the CV curves of the DTDO-based polymers can be explained mainly by differences in porosity, ion-diffusion efficiency, and electronic structure, particularly the HOMO–LUMO energy levels. Porous polymers, such as those incorporating benzene or ethynylbenzene linkers, exhibit enhanced electrochemical performance due to their open frameworks and interconnected pore networks. These features facilitate improved electrolyte penetration and faster ion transport, allowing for greater accessibility to redox-active sites and resulting in more pronounced and broader redox peaks. In contrast, linear polymers with more compact structures restrict ion diffusion pathways, leading to weaker and less defined redox responses.

Moreover, the incorporation of ethynylbenzene units extends the π-conjugation system and lowers the LUMO energy level, which facilitates electron injection and shifts the redox activity to lower potentials (Fig. S13†). The shifts in redox peak positions are also strongly influenced by variations in the band gap energy, which reflect differences in the HOMO (oxidation) and LUMO (reduction) levels. To further understand these electronic effects, we performed density functional theory (DFT) calculations using the B3LYP functional with D3BJ dispersion correction and the 6-31G(d) basis set. As shown in Fig. S13a–d,† the HOMO and LUMO distributions and energy levels were calculated for the Ph-DTDO porous, Ph-DTDO linear, TEPh-DTDO porous, and DEPh-DTDO linear polymers. The results reveal that ethynyl-substituted benzene units reduce the band gap and raise both the HOMO and LUMO levels, thereby

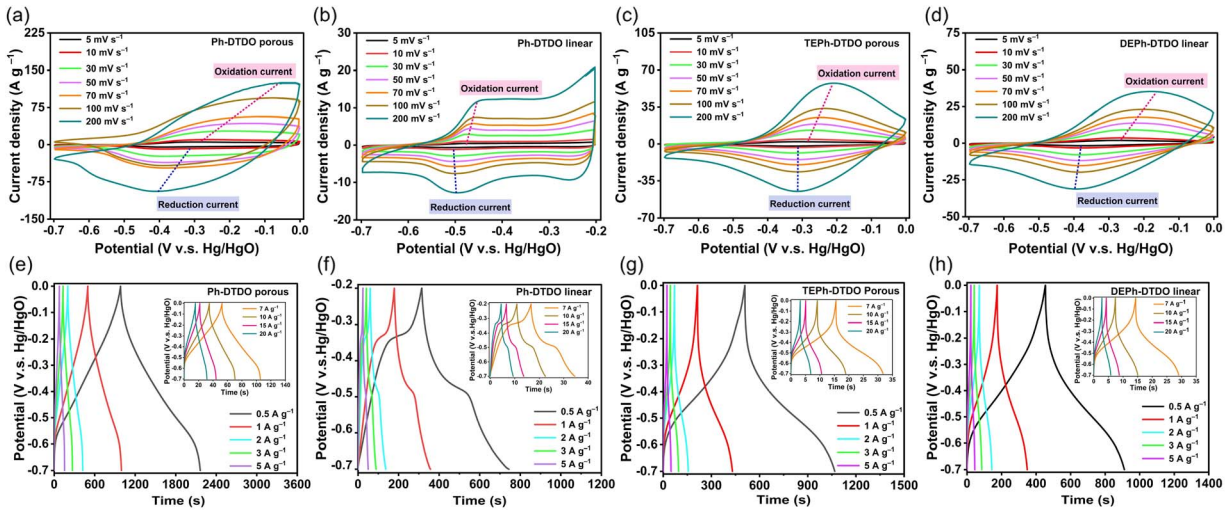

Fig. 4 (a–d) CV profiles of (a) the Ph-DTDO porous, (b) Ph-DTDO linear, (c) TEPh-DTDO porous, and (d) DEPh-DTDO linear polymers, (e–h) GCD curves of (e) the Ph-DTDO porous, (f) Ph-DTDO linear, (g) TEPh-DTDO porous, and (h) DEPh-DTDO linear polymers.

shifting the redox potentials and contributing to the electrochemical differences observed among these polymers. To further evaluate the capacitive performance, GCD measurements were conducted at various current densities ranging from 5 to 200 mV s^{-1} within a potential window of −0.7 to 0 V for all polymer-coated electrodes (Fig. 4e–h). The potential window of −0.7 to −0.2 V was selected for the Ph-DTDO linear polymer as it aligns with the position of its redox peaks (around −0.48 and −0.51 V), ensuring optimal engagement of its Faradaic activity. This range avoids non-Faradaic side reactions that may occur near 0 V, particularly in alkaline media, and results in better GCD curves that accurately reflect its pseudocapacitive behavior. The GCD curves displayed quasi-triangular shapes with slight deviations due to redox contributions, further confirming the pseudocapacitive nature observed in the CV analysis (Fig. 4e–h).[53] To obtain better comparison we combined DTDO polymers at a scan rate of 5 mV s^{-1} for both the CV and GCD curves (Fig. S14a and b†).

The specific capacitances of the Ph-DTDO porous, Ph-DTDO linear, TEPh-DTDO porous, and DEPh-DTDO linear conjugated polymers were determined from discharge times using eqn (S1),† resulting in values of 842.4, 429.2, 399.6, and 327.1 F g^{-1}, respectively, at a current density of 0.5 A g^{-1} (Fig. 5a). These findings demonstrate that incorporating redox-active DTDO units into the polymer framework significantly enhances both energy storage capacity and Faradaic response. Importantly, the results highlight that molecular architecture (porous *vs.* linear) and linker type (benzene and ethynylbenzene) are key factors influencing electrochemical behavior. The Ph-DTDO porous polymer demonstrated the highest specific capacitance at all current densities, with a maximum of 842.4 F g^{-1} at 0.5 A g^{-1} and retaining a significant portion of its capacitance even at 20 A g^{-1}, demonstrating excellent rate performance.[54] This superior performance is primarily attributed to its porous architecture, which facilitates greater electrolyte access and rapid ion diffusion, as well as its benzene linker, which promotes stronger interlayer π–π stacking interactions, enhancing electronic conductivity and redox activity (Fig. S10b†). Comparatively, the Ph-DTDO linear polymer—though incorporating the same benzene linker—showed lower capacitance (429.2 F g^{-1} at 0.5 A g^{-1}), emphasizing the importance of porosity. The lack of a porous structure reduces ion accessibility and restricts the number of active redox sites, thereby limiting its energy storage capacity. Similarly, the TEPh-DTDO porous polymer, despite having a porous structure, exhibited a lower capacitance (399.6 F g^{-1}) than the Ph-DTDO porous polymer. This is due to the presence of the ethynylbenzene linker, which, while promoting planarity and conjugation, results in weaker π–π stacking compared to the benzene linker, thus reducing charge transport efficiency (Fig. S10d†). The DEPh-DTDO linear polymer, which combines both a linear structure and an ethynylbenzene linker, exhibited the lowest capacitance (327.1 F

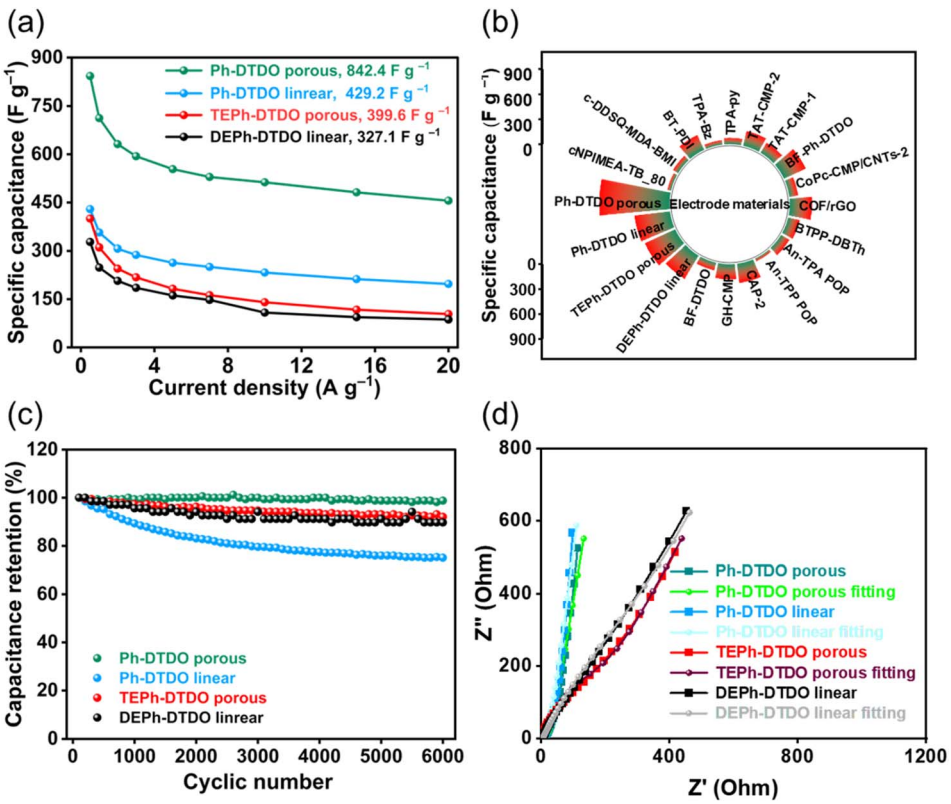

Fig. 5 (a) Specific capacitance values of the Ph-DTDO porous, Ph-DTDO linear, TEPh-DTDO porous, and DEPh-DTDO linear conjugated polymers measured at various current densities. (b) Comparative analysis with previously reported redox-active polymers. (c) Long-term cycling stability evaluated at a current density of 30 A g^{-1} and (d) EIS and corresponding fitted Nyquist plots for the Ph-DTDO porous, Ph-DTDO linear, TEPh-DTDO porous, and DEPh-DTDO linear conjugated polymers.

g^{-1}), further confirming that the synergy between porosity and π-conjugated linker chemistry plays a crucial role in determining the electrochemical performance of conjugated polymers. The resulting specific capacitances of the DTDO-based conjugated polymers are more significant than those of comparable redox-active materials, including COF/rGO (269, at 0.5 A g^{-1}),[54] BTPP-DBTh (143.27 at 0.5 A g^{-1}),[55] BF-DTDO (95.62, at 0.5 A g^{-1}),[36] BF-Ph-DTDO (288.8, at 0.5 A g^{-1}),[36] TAT-CMP-1 (141, at 1 A g^{-1}),[56] TAT-CMP-2 (183, at 1 A g^{-1}),[56] TPA-By (78, at 1 A g^{-1}),[57] TPA-Bz (55.1, at 1 A g^{-1}),[57] BT-PDI (196, at 1 A g^{-1}),[58] c-DDSQ-MDA-BMI (73.6, at 0.5 A g^{-1}),[59] cNPIM EA-TB_80 (46, at 1 A g^{-1}),[60] CoPc-CMP/CNTs-2 (107.2, at 1 A g^{-1}),[61] GH-CMP (182.7, at 0.5 A g^{-1}),[62] CAP-2 (233, at 1 A g^{-1}),[63] An-TPP POP (38.12, at 1 A g^{-1})[64] and An-TPA POP (117.7, at 1 A g^{-1})[64] (Fig. 5b and Table S5†). Consistent with its high capacitance, the endurance of the developed DTDO-based conjugated polymeric electrodes was assessed over 6000 cycles of charging and discharging at a current density of 30 A g^{-1}. Ph-DTDO porous, Ph-DTDO linear, TEPh-DTDO porous, and DEPh-DTDO linear polymers all exhibit exceptional capacitance, retaining 98.78%, 75.07%, 92.06%, and 89.70% of their original specific capacitances, respectively (Fig. 5c). To evaluate the capacitance contribution from the conductive additive multi-walled carbon nanotubes (MW-CNT) used for the electrode slurry preparation, we examined the electrochemical performance (CV and GCD) of the MW-CNT material (Fig. S15a and b†). It demonstrates similar patterns of symmetrical rectangle-shaped CV curves, indicating that the capacitive response is induced by electric double-layer capacitance (EDLC). According to GCD measurements, the estimated specific capacitance is 60.5 F g^{-1} at 0.5 A g^{-1} (Fig. S15c†), significantly lower than that of the DTDO polymers. The capacitive contribution of the MW-CNT materials represents only 7.18% of the Ph-DTDO porous, indicating that it has a minor impact on the electrochemical performance of the studied polymers. The redox mechanism of the DTDO monomer is illustrated in Fig. S16,† involving a two-electron reduction process that generates the $DTDO^{2-}$ anion.[65,66] To verify the proposed redox behavior of the DTDO-based conjugated polymers, CV measurements were conducted for each monomer under consistent conditions, employing a three-electrode configuration in 3 M KOH aqueous electrolyte. The monomers Ph-3B$(OH)_2$, Ph-2B$(OH)_2$, TEPh-3C≡C, and DEPh-2C≡C exhibited nearly rectangular CV profiles (Fig. S17a–e†), characteristic of capacitive behavior. In contrast, the DTDO-2Br monomer showed quasi-reversible redox peaks (Fig. S17c†), highlighting the DTDO moiety as the principal contributor to the redox activity observed in the resulting polymer networks.

To gain deeper insight into the charge storage kinetics of the fabricated electrodes, electrochemical impedance spectroscopy (EIS) was conducted, as it is a standard technique for analyzing ion diffusion rates and the electrical resistance within the electrode material. The EIS measurements were performed at an open-circuit potential with a 5 mV amplitude. As illustrated in Fig. 5d, the Nyquist plots of the DTDO-based polymers exhibited small semicircles in the high-frequency region, indicating efficient electrolyte ion accessibility and minimal charge transfer resistance.[67–69] Besides, at low frequencies, our electrodes displayed nearly vertical lines, indicating their strong capacitive properties.[70] By analyzing the intercept of the Z' axis in the Nyquist plot, the intrinsic ohmic resistance (R_s) can be determined, which reflects the electrical conductivity of the electrodes coated with DTDO-based polymers. The recorded R_s values for the Ph-DTDO porous, Ph-DTDO linear, TEPh-DTDO porous, and DEPh-DTDO linear conjugated polymers were 3.86, 3.94, 3.95, and 6.30 Ω, respectively. The Ph-DTDO porous polymer exhibited a lower R_s value compared to the other polymers, signifying its enhanced conductivity and charge transfer. Fig. S18† presents the corresponding circuit obtained from experimental fitting of Nyquist plots. R_s denotes the ohmic resistance, CPE1 represents the double-layer capacitance at the interface of the electrode and electrolyte, R_{ct} denotes the resistance against charge transfer, and W stands for Warburg impedance. The fitting analysis further reveals that Ph-DTDO porous exhibited the lowest R_s (1.34 Ω) and R_{ct} (79 Ω) (Table S6†), suggesting superior electrochemical performance due to its enhanced conductivity and efficient charge transfer. Conversely, DEPh-DTDO linear displayed the highest R_s (4.47 Ω) and R_{ct} (299 Ω), indicating higher resistance and thus lower performance in charge storage applications. Therefore, Ph-DTDO porous has emerged as the most promising material due to its lower R_s and R_{ct}, demonstrating excellent conductivity and charge transfer efficiency. In addition, the electron conductivity measurements validate the conductivity of our conjugated polymers. The electron conductivity of the DTDO-conjugated polymers was assessed at room temperature using the four-probe technique. The conductivity measurements for the corresponding Ph-DTDO porous, Ph-DTDO linear, TEPh-DTDO porous, and DEPh-DTDO linear conjugated polymers were 5.88, 4.95, 4.57, and 2.51 S cm^{-1}, respectively, confirming their electroconductivity, which is considered to be higher than that of other materials (Table S7†).

To better understand the capacitive behavior of the synthesized DTDO-based conjugated polymers, the relationship between current (i) and scan rate (v) was examined using the power-law expression given in eqn (2).[71,72]

$$i = av^b \quad (2)$$

Since a is a constant, the b value can be determined from the slope of the linear plot of log(i) *versus* log(v). A b value close to 0.5 indicates that the current is proportional to the square root of the scan rate ($i \propto v^{1/2}$), which corresponds to a diffusion-limited Faradaic intercalation mechanism. In contrast, a b value close to 1.0 suggests a surface-controlled capacitive behavior, where the current response scales linearly with the scan rate ($i \propto v$). Fig. 6a–d illustrate that the calculated b value for the DTDO-based conjugated polymers ranged from 0.801 to 0.887 for the anodic peaks and from 0.789 to 0.859 for the cathodic peaks. The results indicated that the simultaneous functioning of diffusion- and capacitance-controlled mechanisms could facilitate the energy storage capabilities of these polymers. Additionally, eqn (3) was used to determine the capacitive contribution to the overall capability.[72,73]

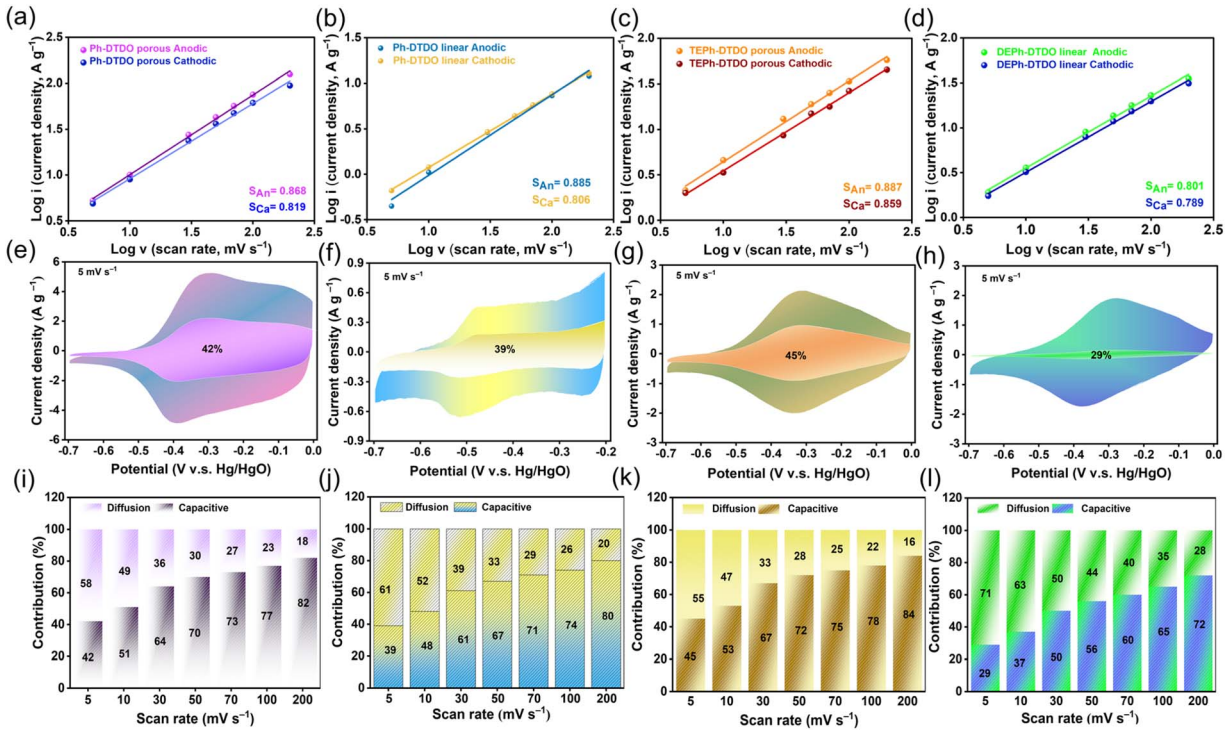

Fig. 6 (a–d) Log(*i*) *versus* log(*v*) plots for the Ph-DTDO porous, Ph-DTDO linear, TEPh-DTDO porous, and DEPh-DTDO linear polymers. (e–h) Capacitive and diffusion-controlled contributions analyzed at 5 mV s^{-1}. (i–l) Charge storage behavior dominated by capacitive and diffusion processes at various scan rates for (e and i) the Ph-DTDO porous, (f and j) Ph-DTDO linear, (g and k) TEPh-DTDO porous, and (h and l) DEPh-DTDO linear polymers.

$$i(V) = k_1 v + k_2 v^{1/2} \quad (3)$$

Here, $i(V)$ represents the current response at a specific potential V, while $k_1 v$ and $k_2 v^{1/2}$ correspond to the contributions from capacitive charge storage and diffusion-controlled processes, respectively. At a scan rate of 5 mV s^{-1}, the capacitive contribution was quantified as 42% for the Ph-DTDO porous polymer, 39% for the Ph-DTDO linear polymer, 45% for the TEPh-DTDO porous polymer, and 29% for the DEPh-DTDO linear polymer, as shown in Fig. 6e–h. These findings suggest that porous polymers show a greater capacitive contribution due to their high surface area and appropriate pore size.[74] Notably, TEPh-DTDO porous exhibited the highest capacitive contribution, suggesting that both porosity and linker design play critical roles in enhancing surface-controlled charge storage. The bar graphs in Fig. 6i–l illustrate the trend in capacitive contribution with increasing scan rates (5–200 mV s^{-1}). In all samples, the capacitive portion increased significantly with scan rate, reaching up to 82% in the Ph-DTDO porous polymer, 80% in the Ph-DTDO linear polymer, 84% in the TEPh-DTDO porous polymer, and 72% in the DEPh-DTDO linear polymer. The decrease in the diffusive part and increase in the capacitive part is due to the ion's interaction time with the electrode material at lower and higher scan rates.[75] These results demonstrate that at higher scan rates, capacitive processes dominate due to the limited time for ion diffusion. Overall, the data confirm that porous architectures and suitable linker structures, particularly in TEPh-DTDO, greatly enhance electrochemical performance by facilitating rapid ion transport and surface redox activity.

To gain deeper insight into the electronic environments and charge distribution of the DTDO-based polymers, molecular electrostatic potential (MESP) maps were analyzed for all four structures: Ph-DTDO porous, Ph-DTDO linear, TEPh-DTDO porous, and DEPh-DTDO linear (Fig. 7). These maps provided a numerical representation of electrophilic and nucleophilic regions, thereby highlighting the most reactive sites within each molecule. Regions of high electron density are depicted in red, while areas of low electron density appear in blue. The Ph-DTDO porous polymer exhibited a highly delocalized and symmetric distribution of the negative potential, particularly around oxygen and sulfur atoms, indicating well-defined redox-active regions and efficient electron delocalization. The highest electron densities, marked by dense red zones, are concentrated near the lone pairs of oxygen atoms, corresponding to the maximum negative potential of −31 kcal mol^{-1} (Fig. 7a). In comparison, the Ph-DTDO linear polymer displayed a slightly less uniform ESP distribution, likely due to its more compact, non-porous structure. Nevertheless, it retained effective charge localization due to the presence of the same phenyl linker, with the highest negative potential also recorded at −31 kcal mol^{-1} on the oxygen atoms (Fig. 7b). The TEPh-DTDO porous polymer shows a marginal decrease in negative potential intensity near its redox-active sites, with a slightly lower maximum value of −30 kcal mol^{-1}, suggesting diminished redox activity despite

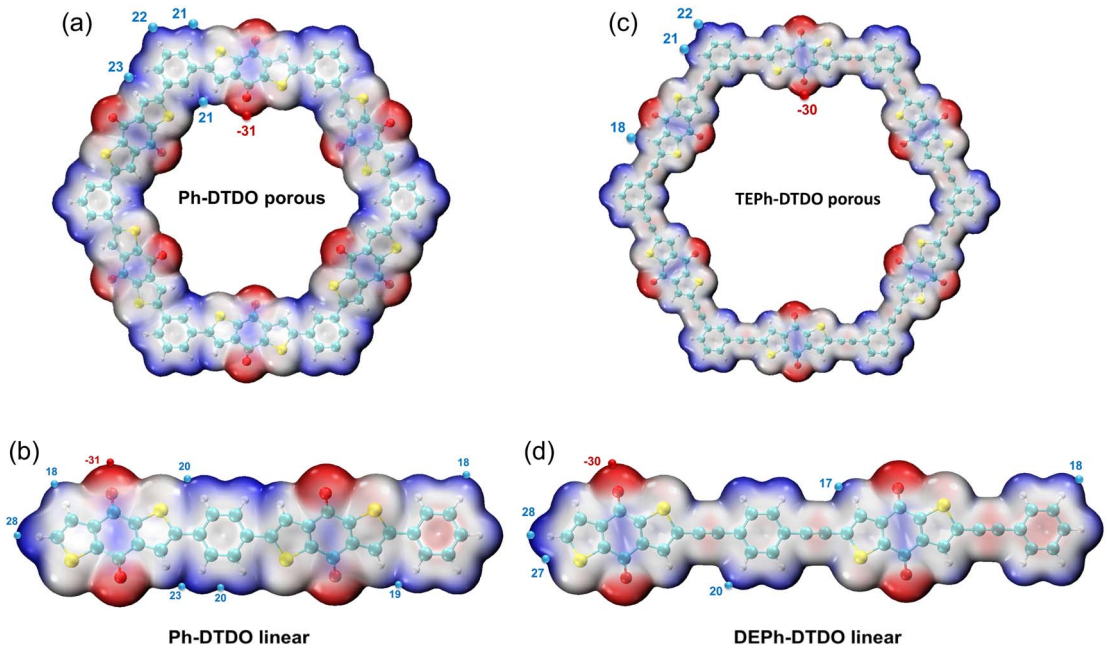

Fig. 7 Molecular electrostatic potential (MESP) colored surface map with ESP surface maxima and minima (in kcal mol^{-1}) for (a) the Ph-DTDO porous, (b) Ph-DTDO linear, (c) TEPh-DTDO porous, and (d) DEPh-DTDO linear polymers calculated at the B3LYP-D3(BJ)/6-31G(d) level. Red color indicates negative potential, and the positive regions are indicated by a blue color.

the presence of porosity (Fig. 7c). Notably, the DEPh-DTDO linear polymer presented the weakest and most irregular ESP distribution, with dispersed negative charge density and limited localization around functional groups. The maximum negative potential in this case is also −30 kcal mol^{-1}, but it is less concentrated and less symmetrically distributed (Fig. 7d). This irregularity reflects poor charge localization and reduces redox efficiency. Overall, these variations in MESP characteristics are consistent with the experimentally observed electrochemical performance of the polymers and underscore the importance of both molecular structure and electronic distribution in governing charge storage behavior.

Overall, the outstanding specific capacitances of the Ph-based polymers (Ph-DTDO porous and Ph-DTDO linear) are attributed to their structural design and superior electronic properties. The phenyl linker contributes to efficient π–π stacking and extended conjugation, enabling superior charge transport. This is further supported by XRD analysis, which reveals a more ordered microstructure with enhanced interlayer packing compared to their ethynylbenzene counterparts. Four-probe conductivity measurements confirm the improved electronic conductivity of the Ph-based polymers, which stems from the synergistic effect of conjugated linkages and effective stacking interactions. The C–S bond content, identified *via* XPS, is notably higher in both the Ph-DTDO porous and Ph-DTDO linear polymers, providing abundant redox-active sites that contribute to faradaic charge storage. Molecular electrostatic potential (MESP) mapping shows a symmetric and delocalized distribution of negative potential, particularly around oxygen and sulfur atoms, indicating efficient charge localization and favorable redox activity. In addition, EIS measurements reveal a lower charge transfer resistance (R_{ct}) and smaller ohmic resistance (R_s), which indicate superior ion diffusion and faster interfacial electron transport in the Ph-based polymers.

In stark contrast, the EPh-DTDO-based polymers (TEPh-DTDO porous and DEPh-DTDO linear) exhibit the lowest specific capacitances due to several compounding limitations. The ethynylbenzene linker disrupts π-conjugation, resulting in a poorly ordered structure as confirmed by XRD, which shows broad and weak diffraction peaks. Four-probe measurements reveal significantly lower conductivity, consistent with the lack of effective orbital overlap and charge delocalization. Furthermore, XPS analysis shows a lower C–S content, indicating fewer redox-active centers. MESP analysis demonstrates irregular and scattered electron density, with negative potential poorly localized around redox-active sites. Finally, EIS data show higher charge transfer resistance and more sluggish ion transport, confirming inefficient electrochemical kinetics.

Furthermore, the higher specific capacitances of the Ph-DTDO porous polymer compared to the Ph-DTDO linear polymer, and of the TEPh-DTDO porous polymer compared to the DEPh-DTDO linear polymer, are attributed to the favorable integration of their porous morphology. Their high porosity, confirmed through nitrogen sorption analysis, offers a large surface area that enhances electrolyte accessibility and facilitates rapid ion diffusion. Taken together, these comprehensive results underscore that well-developed structurally optimized π-conjugated linkers—with high C–S content, good crystallinity, and high conductivity—are critical for achieving high-performance supercapacitor electrodes in conjugated polymer systems.

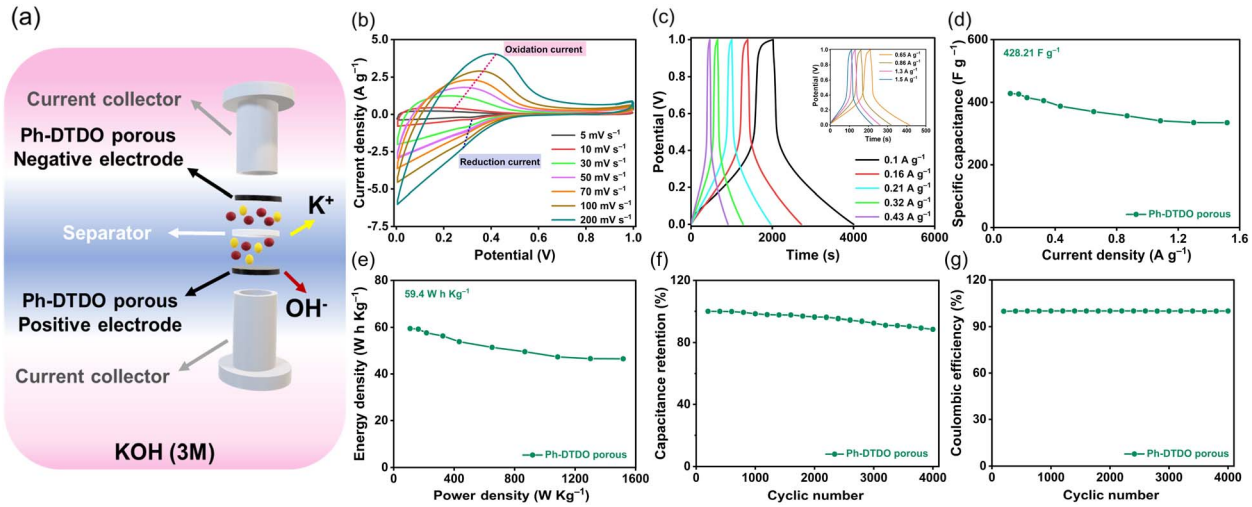

Fig. 8 (a) Schematic illustration of the fabricated SC device based on the Ph-DTDO porous polymer. (b) Cyclic voltammetry (CV) curves recorded at various scan rates. (c) Galvanostatic charge–discharge (GCD) profiles at different current densities. (d) Specific capacitance values as a function of current density. (e) Ragone plot showing the relationship between energy and power densities. (f) Cycling stability over 4000 cycles at a current density of 0.43 A g^{-1}. (g) Coulombic efficiency of the Ph-DTDO porous-based SC device.

The previous results indicate that the Ph-DTDO porous polymer exhibited superior specific capacitance due to several synergistic factors, including the structural stability imparted by the phenyl bridging unit, enhanced surface area and porosity, efficient π–π stacking interactions, a high proportion of electroactive C–S bonds, reduced charge transfer resistance, and improved electrical conductivity. To evaluate the practical applicability of the Ph-DTDO porous polymer as an electrode material for supercapacitor devices, a symmetric supercapacitor (SC) was fabricated using a two-electrode configuration. The device employed 3 M KOH aqueous solution as the electrolyte, with two identical Ph-DTDO porous polymer-based electrodes affixed to carbon sheets and separated by a filter paper membrane (Fig. 8a). CV measurements were performed within a potential window of 0.0 to +1.0 V at scan rates ranging from 5 to 200 mV s^{-1}. The resulting CV curves exhibited nearly rectangular profiles with quasi-reversible redox features that remained stable across the scan range, indicating rapid electrolyte diffusion and efficient charge storage behavior (Fig. 8b). GCD curves recorded at current densities from 0.1 to 1.5 A g^{-1} are presented in Fig. 8c. The specific capacitance values were calculated using the GCD data and eqn (S4),† yielding values of 428.21, 426.49, 414.92, 405.34, 387.60, 370.16, 356.68, 340.73, 335.16, and 334.75 F g^{-1} across the tested current densities (Fig. 8d), thereby confirming the excellent electrochemical performance of the device. Compared with previously reported symmetric porous polymer-based supercapacitors utilizing similar redox-active components, the Ph-DTDO porous-based device demonstrated significantly higher capacitance values (Table S8†).[54,76–81] EIS analysis revealed a small semicircle in the high-frequency region, transitioning into a nearly vertical line in the low-frequency region, indicative of low charge transfer resistance and ideal capacitive behavior (Fig. S19†). The Ragone plot (Fig. 8e) further highlighted the high performance of the device, delivering an energy density of 59.4 W h kg^{-1} at a power density of 108.45 W kg^{-1}. Long-term cycling stability was evaluated *via* GCD measurements over 4000 cycles at a current density of 0.43 A g^{-1}. As shown in Fig. 8f, the device retained 88.51% of its initial capacitance, demonstrating excellent durability. Furthermore, the Coulombic efficiency remained consistently high throughout cycling, ranging between 99.96% and 99.74% (Fig. 8g), further validating the robust and efficient nature of the Ph-DTDO porous-based symmetric supercapacitor.

3. Conclusion

In summary, we have developed a series of redox-active conjugated polymers incorporating benzo[1,2-*b*:4,5-*b*′]dithiophene-4,8-dione (DTDO) units to systematically investigate the roles of porosity and linker architecture in supercapacitor performance. By employing Suzuki and Sonogashira coupling strategies with phenyl-based linkers, we successfully synthesized both porous and linear conjugated polymers, enabling a direct structure–property correlation. The two types of porous polymers (Ph-DTDO porous and TEPh-DTDO porous) were synthesized through the Suzuki and Sonogashira coupling reactions of DTDO-2Br with Ph-3B$(OH)_2$ and TEPh-3C≡C, respectively. In contrast, the two types of linear polymers (Ph-DTDO linear and DEPh-DTDO linear) were synthesized using the Suzuki and Sonogashira coupling reactions of DTDO-2Br with Ph-2B$(OH)_2$ and TEPh-2C≡C, respectively. Among them, the Ph-DTDO porous polymer displayed a surface area of 62.7 m^2 g^{-1}, strong π–π stacking interactions, and outstanding electrical conductivity of 5.88 S cm^{-1}. It delivered a high specific capacitance of 842.4 F g^{-1} at a current density of 0.5 A g^{-1} in a three-electrode configuration and retained 98.78% of its capacitance after 6000 charge–discharge cycles, demonstrating outstanding cycling stability. In a symmetric supercapacitor setup, the same

material achieved a specific capacitance of 428.21 F g^{-1} and an energy density of 59.4 W h kg^{-1}. Notably, 88.51% of the initial capacitance was preserved after 4000 cycles, confirming its robust long-term performance. These findings highlight the critical influence of porous architecture, π–π stacking, and charge-transfer pathways facilitated by molecular linkers. This work provides valuable design principles for tailoring redox-active frameworks in organic polymer-based energy storage devices, offering new avenues for high-performance and sustainable supercapacitor materials.

Data availability

Data is contained within the article or ESI.†

Conflicts of interest

There are no conflicts to declare.

Acknowledgements

This study was supported financially by the Ministry of Science and Technology, Taiwan, under contracts NSTC 112-2221-E-110-005-MY3 and 113-2218-E-110-004-.

References

1 M. Mouselly, H. Alawadhi and S. T. Senthilkumar, *Curr. Opin. Electrochem.*, 2024, **48**, 101581.
2 S. Shruti, M. Mohanraj, S. Senthilkumar and M. Ulaganathan, *Curr. Opin. Electrochem.*, 2024, **47**, 101557.
3 A. Ali, S. Ahmed, W. Jiang, G. Park and S. J. Oh, *Curr. Opin. Electrochem.*, 2025, **50**, 101640.
4 S. Xing, N. Liu, Q. Li, M. Liang, X. Liu, H. Xie, F. Yu and J. Ma, *Nat. Commun.*, 2024, **15**, 4951.
5 H. Zhang, Y. Luo, J. Zhou, L. Wang, L. Shu, W. He, Q. Zhang and P. Wang, *Nano Lett.*, 2024, **24**, 10131–10138.
6 N. Singh, V. Singh, N. Bisht, P. Negi, A. Dhyani, R. K. Sharma and B. S. Tewari, *J. Energy Storage*, 2025, **121**, 116498.
7 Z. Wang, C. Wang, Y. Chen and L. Wei, *Adv. Mater. Technol.*, 2023, **8**, 2201828.
8 F. Mashkoor, M. Shoeb, S. Zhu, J. Ahmed, S. M. Noh and C. Jeong, *Surf. Interfaces*, 2025, **62**, 106198.
9 Z. Fu, H. Zhang, D. Geng, Z. Liu, Z. Zhang, X. Li and C. Yan, *Adv. Energy Mater.*, 2025, **15**, 2403934.
10 H. W. Park and K. C. Roh, *J. Power Sources*, 2023, **557**, 232558.
11 C. V. M. Gopi, S. Alzahmi, M. Y. Al-Haik, Y. A. Kumar, F. Hamed, Y. Haik and I. M. Obaidat, *Mater. Today Sustain.*, 2024, **28**, 100981.
12 S. A. Patil, P. B. Jagdale, A. Sfeir, M. Pathak, S. Royer, A. K. Samal, C. S. Rout and M. Saxena, *J. Energy Storage*, 2025, **121**, 116526.
13 C. Debbarma, S. Radhakrishnan, S. M. Jeong and C. S. Rout, *J. Mater. Chem. A*, 2024, **12**, 18674–18704.
14 I. Hussain, M. Kathiresan, K. Singh, B. Kalidasan, A. C. Mendhe, M. N. Islam, K. Meng, M. K. Aslam, M. B. Hanif, W. Al Zoubi and K. Zhang, *InfoMat*, 2025, **7**, e70011.
15 Y. Shao, M. F. El-Kady, J. Sun, Y. Li, Q. Zhang, M. Zhu, H. Wang, B. Dunn and R. B. Kaner, *Chem. Rev.*, 2018, **118**, 9233–9280.
16 S. Kanthasamy, T. Doulassiramane, R. Padmanaban and S. Thangavelu, *Electrochim. Acta*, 2025, **518**, 145789.
17 R. T. Yadlapalli, R. R. Alla, R. Kandipati and A. Kotapati, *J. Energy Storage*, 2022, **49**, 104194.
18 Z. Lu, R. Raad, F. Safaei, J. Xi, Z. Liu and J. Foroughi, *Front. Mater. Sci.*, 2019, **6**, 138.
19 M. H. Gharahcheshmeh and K. Chowdhury, *Energy Adv.*, 2024, **3**, 2668.
20 B. M. Mahimai, E. Li, J. Pang, J. Zhang and J. Zhang, *J. Energy Storage*, 2024, **96**, 112598.
21 A. F. Saber, K. Y. Chen, A. F. M. EL-Mahdy and S. W. Kuo, *J. Polym. Res.*, 2021, **28**, 430.
22 D. Zhou, K. Zhang, S. Zou, X. Li and H. Ma, *J. Mater. Chem. A*, 2024, **12**, 17021–17053.
23 W. Liu, Y. Yang, L. Guo, J. Di, C. H. Lau, M. V. Bermeshev and L. Shao, *Chem. Eng. J.*, 2024, **498**, 155569.
24 L. R. Ahmed, L. Gilmanova, C. T. Pan, S. Kaskel and A. F. M. EL-Mahdy, *ACS Appl. Polym. Mater.*, 2022, **4**, 9132–9143.
25 X. Cui, M. Wu, X. Liu, B. He, Y. Zhu, Y. Jiang and Y. Yang, *Chem. Soc. Rev.*, 2024, **53**, 1447–1494.
26 T. F. Huang, Y. R. Zhuang, C. L. Chang, C. L. Huang, W. C. Lin, Z. C. Jiang, L. Y. Ting, I. M. Mekhemer, Y. E. Sun, P. Kidkhunthod, J. L. Chen, Y. C. Huang, H. K. Hsu, Y. T. Tseng, Y. H. Wu, B. H. Li, S. D. Yang, Y. J. Cheng and H. H. Chou, *J. Mater. Chem. A*, 2024, **12**, 3633–3643.
27 M. Xu, C. Wei, Y. Zhang, J. Chen, H. Li, J. Zhang, L. Sun, B. Liu, J. Lin, M. Yu, L. Xie and W. Huang, *Adv. Mater.*, 2024, **36**, 2301671.
28 L. R. Ahmed, C. H. Chuang, J. Lüder, H. W. Yang and A. F. M. EL-Mahdy, *Macromolecules*, 2022, **55**, 10197–10209.
29 X. Xia, L. Tian, R. Ji, N. Li, D. Chen, H. Li, J. Jiang, Q. Xu and J. Lu, *Chem. Eng. Sci.*, 2024, **285**, 119555.
30 J. H. Wang, C. L. Chang, Z. W. Zhang and A. F. M. EL-Mahdy, *Polym. Chem.*, 2022, **13**, 5300–5308.
31 J. H. Wang, A. E. Hassan, A. M. Elewa and A. F. M. EL-Mahdy, *J. Mater. Chem. A*, 2024, **12**, 14005–14021.
32 Z. Genene, Z. Xia, G. Yang, W. Mammo and E. Wang, *Adv. Mater. Technol.*, 2024, **9**, 2300167.
33 G. Quek, D. Ohayon, P. R. Ng and G. C. Bazan, *Small*, 2024, **20**, 2401395.
34 H. Sun, J. Li, W. Liang, X. Gong, A. Jing, W. Yang, H. Liu and S. Ren, *Small Methods*, 2024, **8**, 2301335.
35 A. F. Saber and A. F. M. EL-Mahdy, *New J. Chem.*, 2021, **45**, 21834–21843.
36 S. X. Liao and A. F. M. EL-Mahdy, *ACS Appl. Energy Mater.*, 2025, **8**, 3074–3086.
37 A. F. Saber, S. U. Sharma, J. T. Lee, A. F. M. EL-Mahdy and S. W. Kuo, *Polymer*, 2022, **254**, 125070.
38 M. H. Gharahcheshmeh and K. Chowdhury, *Adv. Mater. Interfaces*, 2024, **11**, 2400118.

39 Y. Liu, Y. Xie, X. Liu, G. Huang and C. Liang, *Fuel*, 2024, **366**, 131415.
40 Y. Zang, Y. Yu, Y. Chen, M. Fan, J. Wang, J. Liu, L. Xu, H. Jia and S. Dong, *Chem. Eng. J.*, 2024, **484**, 149709.
41 Y. Gu, W. Li, Y. Zheng, B. Zhu, J. Shi and W. Tang, *Chem. Eng. J.*, 2025, **508**, 161040.
42 L. Liang, J. T. Wang, C. Y. Mei and W. S. Li, *Polymer*, 2013, **54**, 2278–2284.
43 S. Uppugalla, R. Pothu, R. Boddula, M. A. Desai and N. Al-Qahtani, *Emerg. Mater.*, 2023, **6**, 1167–1176.
44 M. Yi, X. Chen, S. Wu, J. Ge, X. Zhou and G. Yin, *Polymers*, 2018, **10**, 1006.
45 Y. Oaki and K. Sato, *RSC Appl. Polym.*, 2025, **3**, 78–91.
46 G. Chen, Z. Zhou, J. Liu, X. Yang, F. Wu, X. Zhong, X. Han, J. Liu and X. Jiang, *Fuel*, 2025, **381**, 133699.
47 W. R. Wang, J. Li, Q. Li, Z. W. Xu, L. N. Liu, X. Q. Chen, W. J. Xiao, J. Yao, F. Zhang and W. S. Li, *J. Mater. Chem. A*, 2021, **9**, 8782–8791.
48 Q. Li, K. H. Li, L. N. Liu, Z. X. Xue, Z. W. Xu and W. S. Li, *ACS Appl. Polym. Mater.*, 2023, **5**, 8570–8578.
49 X. Zhao, P. Pachfule, S. Li, T. Langenhahn, M. Ye, C. Schlesiger, S. Praetz, J. Schmidt and A. Thomas, *J. Am. Chem. Soc.*, 2019, **141**, 6623–6630.
50 R. Sugiura, H. Imai and Y. Oaki, *Nanoscale Adv.*, 2024, **6**, 1084–1090.
51 S. You, Z. Ding, R. Yuan, J. Long and C. Xu, *J. Colloid Interface Sci.*, 2024, **664**, 63–73.
52 R. Li, J. Li, Q. Liu, T. Li, D. Lan and Y. Ma, *Adv. Compos. Hybrid Mater.*, 2025, **8**, 86.
53 J. F. Gao, J. F. Hou and L. B. Kong, *Electrochim. Acta*, 2023, **439**, 141692.
54 C. Li, J. Yang, P. Pachfule, S. Li, M. Y. Ye, J. Schmidt and A. Thomas, *Nat. Commun.*, 2020, **11**, 4712.
55 S. Abdelnaser, S. W. Kuo and A. F. M. EL-Mahdy, *J. Power Sources*, 2025, **635**, 236535.
56 X. C. Li, Y. Zhang, C. Y. Wang, Y. Wan, W. Y. Lai, H. Pang and W. Huang, *Chem. Sci.*, 2017, **8**, 2959–2965.
57 M. G. Kotp, S. U. Sharma, J. T. Lee, A. F. M. EL-Mahdy and S. W. Kuo, *J. Taiwan Inst. Chem. Eng.*, 2022, **134**, 104310.
58 S. K. Pati, D. Patra, S. Muduli, S. Mishra and S. Park, *J. Mater. Chem. A*, 2024, **12**, 21165–21175.
59 Z. Y. Chen, W. C. Chen and S. W. Kuo, *Polym. Chem.*, 2024, **15**, 553–564.
60 J. W. Jeon, J. Shin, J. Lee, J. H. Baik, R. Malpass-Evans, N. B. McKeown, T. H. Kim, J. C. Lee, S. K. Kim and B. G. Kim, *Appl. Surf. Sci.*, 2020, **530**, 147146.
61 L. Mei, X. Cui, Q. Duan, Y. Li, X. Lv and H. G. Wang, *Int. J. Hydrogen Energy*, 2020, **45**, 22950–22958.
62 M. Zhang, T. Zhao, J. Dou, Z. Xu, W. Zhang, X. Chen, X. Wang and B. Zhou, *Chemelectrochem*, 2019, **6**, 5946–5950.
63 W. Liu, M. Ulaganathan, I. Abdelwahab, X. Luo, Z. Chen, S. J. R. Tan, X. Wang, Y. Liu, D. Geng, Y. Bao, J. Chen and K. P. Loh, *ACS Nano*, 2018, **12**, 852–860.
64 A. F. Saber, S. Abdelnaser, A. F. M. EL-Mahdy and S. W. Kuo, *Electrochim. Acta*, 2025, **511**, 145397.
65 J. Zhan and A. F. M. EL-Mahdy, *Chem. Eng. J.*, 2023, **473**, 145124.
66 T. A. Gaber, L. R. Ahmed and A. F. M. EL-Mahdy, *J. Mater. Chem. A*, 2023, **11**, 19408–19417.
67 K. A. Kumar, A. Pandurangan, S. Arumugam and M. Sathiskumar, *Sci. Rep.*, 2019, **9**, 1228.
68 A. C. Lazanas and M. I. Prodromidis, *ACS Meas. Sci. Au*, 2023, **3**, 162–193.
69 N. Loew, H. Watanabe, I. Shitanda and M. Itagaki, *Electrochim. Acta*, 2022, **421**, 140467.
70 K. Li, X. Liu, T. Zheng, D. Jiang, Z. Zhou, C. Liu, X. Zhang, Y. Zhang and D. Losic, *Chem. Eng. J.*, 2019, **370**, 136–147.
71 L. Kang, S. Liu, Q. Zhang, J. Zou, J. Ai, D. Qiao, W. Zhong, Y. Liu, S. C. Jun, Y. Yamauchi and J. Zhang, *ACS Nano*, 2024, **18**, 2149–2161.
72 V. S. Bhat, A. Toghan, G. Hegde and R. S. Varma, *J. Energy Storage*, 2022, **52**, 104776.
73 Y. Liu, L. Zhou, J. Ouyang, X. Ao, M. Shuang and A. A. Adesina, *Sep. Purif. Technol.*, 2024, **334**, 125989.
74 R. Heimböckel, F. Hoffmann and M. Fröba, *Phys. Chem. Chem. Phys.*, 2019, **21**, 3122–3133.
75 M. Z. Iqbal, M. M. Faisal, M. Sulman, S. R. Ali, A. M. Afzal, M. A. Kamran and T. Alharbi, *J. Energy Storage*, 2020, **29**, 101324.
76 H. Zuo, J. Duan, B. Lyu, W. Lyu, Y. Li, X. Mei and Y. Liao, *Macromol. Rapid Commun.*, 2024, **45**, 2300238.
77 K. Gajewska, A. Moyseowicz, D. Minta and G. Gryglewicz, *J. Mater. Sci.*, 2023, **58**, 1721–1738.
78 Y. Liao, H. Wang, M. Zhu and A. Thomas, *Adv. Mater.*, 2018, **30**, 1705710.
79 A. F. Saber, Y. F. Chen, L. Mabuti, S. V. Chaganti, S. U. Sharma, J. Lüder, J. T. Lee, S. W. Kuo and A. F. M. EL-Mahdy, *Mater. Adv.*, 2025, **6**, 607–616.
80 Y. Zhao, F. Xie, C. Zhang, R. Kong, S. Feng and J. X. Jiang, *Microporous Mesoporous Mater.*, 2017, **240**, 73–79.
81 W. Lyu, C. Yan, Z. Chen, J. Chen, H. Zuo, L. Teng, H. Liu, L. Wang and Y. Liao, *ACS Appl. Energy Mater.*, 2022, **5**, 3706–3714.